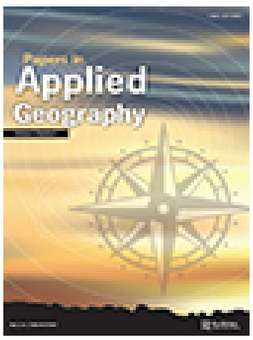

Routledge
Taylor & Francis Group

Papers in Applied Geography

ISSN: (Print) (Online) Journal homepage: https://www.tandfonline.com/loi/rpag20

Deriving Land and Water Surface Elevations in the Northeastern Yucatán Peninsula Using PPK GPS and UAV-Based Structure from Motion

Thomas J. Pingel , Andrea Saavedra & Lillian Cobo

To cite this article: Thomas J. Pingel , Andrea Saavedra & Lillian Cobo (2021): Deriving Land and Water Surface Elevations in the Northeastern Yucatán Peninsula Using PPK GPS and UAV-Based Structure from Motion, Papers in Applied Geography

To link to this article: https://doi.org/10.1080/23754931.2021.1871937

Published online: 02 Feb 2021.

PAPERS IN APPLIED GEOGRAPHY
https://doi.org/10.1080/23754931.2021.1871937

Routledge
Taylor & Francis Group

Deriving Land and Water Surface Elevations in the Northeastern Yucatán Peninsula Using PPK GPS and UAV-Based Structure from Motion

Thomas J. Pingel[a], Andrea Saavedra[b], and Lillian Cobo[c]

[a]Department of Geography, Virginia Polytechnic Institute and State University, Blacksburg, Virginia, USA; [b]Department of Earth Science, Northeastern Illinois University, Chicago, Illinois, USA; [c]Department of Geographic and Atmospheric Sciences, Northern Illinois University, DeKalb, Illinois, USA

ABSTRACT

While UAV-based imaging methods such as drone lidar scanning (DLS) and Structure from Motion (SfM) are now widely used in geographic research, accurate water surface elevation (WSE) measurement remains a difficult problem, as water absorbs wavelengths commonly used for lidar and SfM feature matching fails on these dynamic surfaces. We present a methodology for measuring WSE in a particularly challenging environment, the Yucatán Peninsula, where cenotes – exposed, water-filled sinkholes – provide an observation point into the critically important regional groundwater supply. In the northeastern Yucatán, elevations are very close to sea level, the area is of low relief, and the near-vertical edges of the walls of the cenotes complicate the use of the so-called "water edge" technique for WSE measurement. We demonstrate how post-processing kinematic (PPK) correction of even a single Real Time Kinematic (RTK) Global Positioning System (GPS) unit can be used to finely register the SfM-derived point cloud, and present evidence from both simulations and an empirical study that quantify the effect of "dip" in SfM-based environmental reconstructions. Finally, we present a statistical analysis of the problem of "thick" or "fuzzy" point clouds derived from SfM, with particular emphasis on their interactions with WSE measurement.

KEYWORDS

Unmanned aerial systems; unmanned aerial vehicles; Structure from Motion (SfM); photogrammetry; water surface elevation

Introduction

The Yucatán Peninsula in southeastern Mexico has experienced rapid growth in both tourism and resident population in the last several decades, leading to increased pressure on water resources in the region (Pi-Sunyer and Thomas 2015). The geology of the coastal region of the peninsula features an extraordinarily low relief karst landscape, where the most abundant surface water features are cenotes – collapsed sinkholes that provide direct access to groundwater. Cenotes have historically been used for fresh water extraction, but have more recently been used for eco-tourism and recreation (Munro and Melo Zurita 2011). They have also proven to be scientifically valuable, as they provide a ready resource for monitoring groundwater quality and flow in the region (Perry, Velazquez-Oliman, and Marin 2002; Perry, Velazquez-Oliman, and Socki 2003). Recently, Bandini *et al.* (2018, 2020) demonstrated how unmanned aerial vehicles (UAVs) can be used to monitor cenotes in the Yucatán, and we extend that work by closely examining how real-time and post-processing kinematic global positioning system (RTK/PPK GPS) units can be used

CONTACT Thomas J. Pingel tpingel@vt.edu Department of Geography, Virginia Polytechnic Institute and State University, Blacksburg, VA, USA.

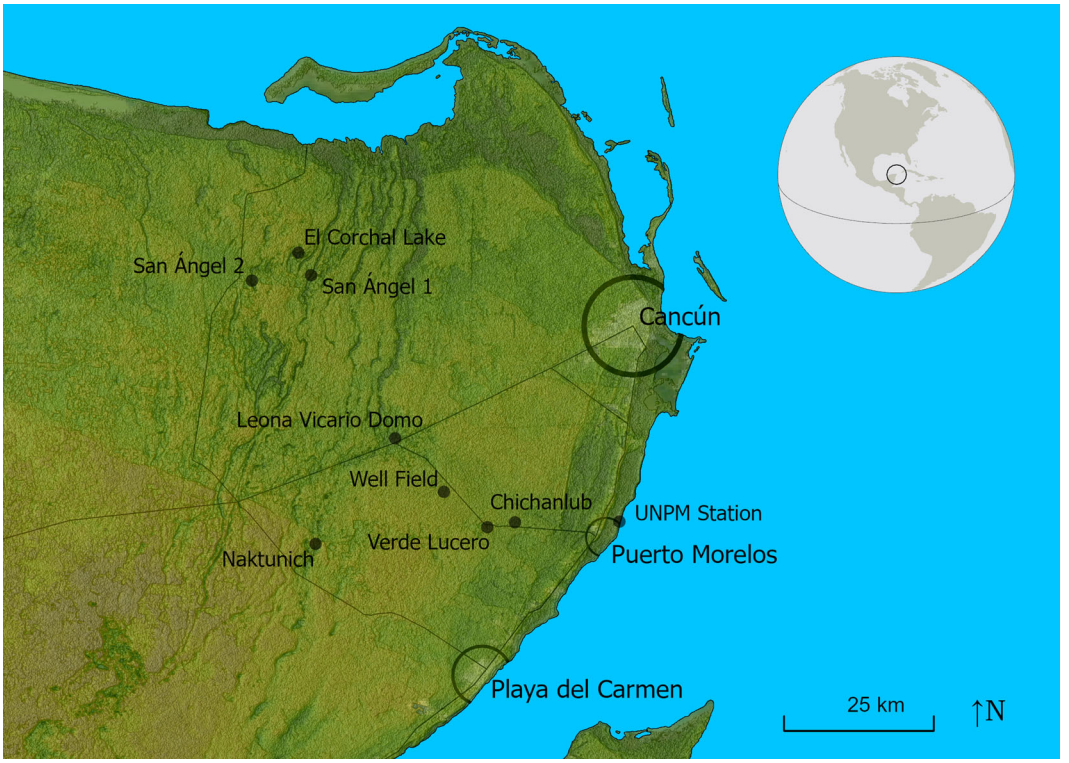

Figure 1. Shaded Relief of the study area in the NE Yucatán Peninsula. Gray lines show major regional roads. Circles show coastal cities near the study area.

in tandem with UAVs in these environments, where flying, imaging, and accurate GPS use are confounded by the extremely low relief and thick vegetation that often surrounds the cenotes.

Our specific research questions are:

1. What techniques can improve the accuracy of water surface elevation (WSE) measurements from photogrammetric Structure-from-Motion (SfM) point clouds?
2. How can Ground Control Points (GCP) derived from consumer-grade RTK GPS units be more maximally leveraged to correct and evaluate SfM reconstructions, so that fewer points are needed?
3. How does an improved knowledge of WSEs in the study region south of Cancún inform our understanding of the regional groundwater flow model?

The first question is critically important, as comparisons of SfM-based methods to active sensors is ongoing (*e.g.*, Bandini *et al.* 2020); for a fair comparison, processing techniques need to be as advanced and accurate as possible. Further, both dense vegetation and the steep sides of cenotes make traditional SfM WSE approaches difficult. The second question is critical for some environments; while onsite GCP network construction and use is still recommended practice when possible, they are expensive and time consuming to create, and may be impractical in some environments. In our case, the extremely thick vegetation surrounding the cenotes we examined made their use impossible in most cases. Finally, our study is part of a larger investigation into groundwater flow and quality in the area (Leal-Bautista *et al.* 2019; Casas-Beltrán *et al.* 2020; McKay, Lenczewski, and Leal-Bautista 2020), to which our WSE measurements are a contribution. We wanted to utilize these methods to contribute to the consensus groundwater flow model

(Perry, Velazquez-Oliman, and Socki 2003) of the study region south of Cancún (Figure 1), where flow directions are notably uncertain owing to the low relief and highly fractured rock.

Because groundwater flows are strongly influenced by surface elevations (Condon and Maxwell 2015), DEMs are widely used as part of groundwater models. However, global DEMs such as the SRTM and ASTER GDEM2 datasets are also not well suited for hydrological modeling when relief is very low (Bhang and Schwartz 2008). Lidar would likely provide a sufficiently accurate representation of the terrain even in this low-relief area (Jones *et al.* 2008), but no publicly available lidar dataset for the northeastern Yucatán is yet available. For larger bodies of water (large lakes and rivers with rivers greater than 100 m), the upcoming 2021 Surface Water Open Topography (SWOT) mission promises to provide decimeter accuracy (Biancamaria, Lettenmaier, and Pavelsky 2016; Bandini *et al.* 2020), but small cenotes of the type described in this study would not be measured.

For these reasons, many have turned to more sophisticated GPS units (sometimes more precisely referred to as Global Navigation Satellite System or GNSS units to describe the ability of these units to use more than just the United States based GPS constellation), more recently, to aerial imaging via unmanned aerial vehicle (UAV) or drone. Survey grade GPS units that use additional GPS broadcast bands to compute their position offer potentially much higher precision than consumer units (Wing, Ecklund, and Kellog 2005), with nominal accuracies of 1 cm (horizontal) and 2 cm (vertical). In practice, these units tend to be prohibitively expensive for many researchers, and actual accuracy in less-than-ideal conditions can be substantially worse than the units themselves estimate (though still less than a meter; Andersen *et al.* 2009). Differential GPS (DGPS), in which a nearby GPS correction station is used to correct a client unit, can similarly reduce error (Marín *et al.* 2008). Satellite Based Augmentation Systems (SBAS) broadcast these corrections, and many consumer-grade GPS units receive and apply these corrections automatically to reduce total error to 1–2 m (Andersen *et al.* 2009; Heßelbarth and Wanninger 2013).

Real-time Kinematic (RTK) GPS units function similarly to DGPS, with one unit (the base) providing corrections to one or more nearby receiving units (rovers). Corrections are made relative to the base station; if the base station's position is known (*e.g.*, is placed at a previously surveyed location) then the relative precision of the corrections (nominally 1 cm horizontal and 2 cm vertical) can be translated to enhanced accuracy of absolute position. Low-cost commercial RTK GPS units, such as the one used in this study (the single-band Emlid Reach, $250) can be used together or in combination with the Continuously Operating Reference Stations (CORS) network. Hill (2019) extensively tested consumer-grade RTK GPS receivers (the single-band Emlid Reach RS) and found that they were accurate to within 1 cm of much more expensive (> $10,000) Leica GS15 dual-frequency units. The units also provide output data that can be post-processed via the open-source *rtklib* package, or submitted to online processing centers such as the National Geodetic Survey's OPUS or National Resource Canada's PPP service. Several recent studies have demonstrated the efficacy of UAV-mounted RTK GPS for direct image georeferencing (Stöcker *et al.* 2017; Forlani *et al.* 2018). Real time correction methods produce measurements that are high in relative but not absolute accuracy unless tied to a previously surveyed point and require the placement of a "base" RTK GPS unit that locally transmits its corrections via a Bluetooth, WiFi, LoRa, or NTRIP server. In contrast, Post-Processing Kinematic (PPK) GPS correction methods can use nearby stations (*e.g.*, Continuously Operating Reference or CORS stations) or secondary RTK GPS devices that are not directly in real-time communication with the aircraft to achieve similar results and with less sensitivity to local communication error (Zhang *et al.* 2019).

While GPS units provide point-based measurements, drone-based Structure from Motion (SfM) provides a much larger areal measurement of local topography and has been applied to a wide variety of geographical contexts (Lucieer, de Jong, and Turner 2014; Turner, Lucieer, and Watson 2012; Mancini *et al.* 2013; Wallace *et al.* 2016). SfM is process arising from the computer vision community whereby multiple images of the same object or location are automatically

compared, algorithmically feature-matched, and combined to render 3 D representations (Spetsakis and Aloimonos 1991; Szeliski and Kang 1994; Snavely, Seitz, and Szeliski 2008). When images are captured using a UAV, they are often geotagged with GPS to improve the feature-matching process and to correctly scale and orient the digital reconstruction with respect to real space, aiding in the production of conventional geographic products such as point clouds, orthophotos, and digital surface and terrain models for secondary geospatial analysis (Westoby *et al.* 2012; Dandois and Ellis 2010; Eltner *et al.* 2016). Software implementing SfM has rapidly advanced from Microsoft Photosynth, which was based on the work of Snavely, Seitz, and Szeliski (2008) to widely used commercial applications such as Agisoft Photoscan (now Metashape), Pix4D, and RealityCapture (Jiang, Jiang, and Jiang 2020). SfM is also now widely available in open source packages such as OpenDroneMap and AliceVision/Meshroom, and computational SfM toolkits available for OpenCV and Matlab. The availability of the tools combined with the inexpensive deployment of cameras via small UAVs has led to a large number of studies employing UAS/SfM in diverse areas including natural and urban forestry (Dandois and Ellis 2010; Wallace *et al.* 2016; Iglhaut *et al.* 2019; Isibue and Pingel 2020), coastal monitoring (Brunier *et al.* 2016; Turner, Harley, and Drummond 2016; Scarelli *et al.* 2017; Burdziakowski *et al.* 2020), natural disaster damage assessment (de Roos *et al.* 2018; Udo, Takeda, and Koshimura 2018; Womble, Wood, and Mohammadi 2018; Anders *et al.* 2020; Gesch *et al*), archaeology (Verhoeven *et al.* 2012; Hill 2019; Nesbit and Hugenholtz 2019) and many more.

Although Structure from Motion can produce excellent results, it is also prone to several problems. James and Robson (2014) documented a "doming" effect in reconstructions in which surfaces appear convex or concave. This happens as a result of poorly calibrated camera models where focal length, and radial and tangential distortion parameters are improperly estimated. The so-called rolling shutter in inexpensive and lightweight digital cameras often used in UAV photography exacerbates this issue. Second, unlike lidar, cameras are passive sensors and can only penetrate through tree cover to the degree that gaps in the canopy allow (Eltner *et al.* 2016; Wallace *et al.* 2016). As automated feature matching is used to locate the same object in pairs of overlapping images, relatively featureless terrain such as snow packs (Fernandes *et al.* 2018; Filhol *et al.* 2019) and highly irregularly shaped environments such as forest canopies may require special attention to mission planning parameters and subsequent image processing (Frey *et al.* 2018). Water features are particularly problematic to recover via SfM, as the moving surface and reflections can make accurate reconstruction extremely error prone or impossible (Harwin and Lucieer 2012; Rosnell and Honkavaara 2012; Flener *et al.* 2013; Bandini, Butts, *et al.* 2017). SfM can further be impeded by variables such as water turbidity, atmospheric conditions, camera distortion, and thick vegetation (Harwin and Lucieer 2012; Rosnell and Honkavaara 2012; Bandini, Butts, *et al.* 2017). Other highly homogenous environments pose similar problems for SfM reconstruction as automated feature-matching between images fails (Mancini *et al.* 2013; Ryan *et al.* 2015; Wallace *et al.* 2016; Fernandes *et al.* 2018; Frey *et al.* 2018; Filhol *et al.* 2019; Meyer and Skiles 2019).

While field water surface elevations (WSE) are conventionally measured using traditional surveying techniques such as through the use of a total station or similar equipment (Marín *et al.* 2008) or by using a line leveling approach (Bandini *et al.* 2020), recently UAVs have been used to monitor water surface elevations (WSE) of inland water bodies such as rivers and lakes using a variety of passive and active sensor platforms. UAV-based WSE measurement has the potential to provide more continuous profiles of water bodies than other methods such as spaceborne observations, as well as improve both spatial and temporal resolution (Bandini, Butts, *et al.* 2017). Radar has shown the most promise for very accurately sensing WSE (RMSE = 3 cm) compared to conventional SfM (RMSE = 18–45 cm) and lidar-based (RMSE = 22 cm) techniques, and with shorter surveying and processing time (Bandini, Jakobsen, *et al.* 2017; Bandini, Lopez-Tamayo, *et al.* 2018; Bandini *et al.* 2019; Bandini *et al.* 2020). However, these techniques still require

customized equipment and are not yet widely available to researchers. SfM-based approaches to WSE cannot measure the water surface directly, as the dynamic surface prevents conventional feature matching algorithms from finding stable keypoints between images, and still water results in reflections that confound reconstruction (Bandini *et al.* 2020). Smaller Drone Laser Scanning (DLS) systems can image small water bodies and the surrounding areas at much higher resolution than traditional aerial lidar, but the cost of such units can be prohibitively expensive (Resop, Lehmann, and Hession 2019).

Westaway, Lane, and Hicks (2003) demonstrated the efficacy of SfM using aerial photographs taken from a conventional aircraft using an extensive network of manually placed Ground Control Points (GCPs) to register the images. Many researchers have recently used small UAS and SfM workflows to model sections of small rivers and streams (Flener *et al.* 2013; Javernick, Brasington, and Caruso 2014). In these cases, large networks of GCPs were used to finely register the images. WSE elevations were derived from using the land-water interface (the so-called "water-edge" technique, Bandini *et al.* 2020) using minimum or minimum-quartile methods applied to interpolated Digital Elevation Models (Javernick, Brasington, and Caruso 2014; Woodget *et al.* 2015; Pai *et al.* 2017). Javernick, Brasington, and Caruso (2014) found that steep slopes of the surrounding water edge (as in the case with the cenotes in our study area) proved particularly problematic to accurately measure.

During a typical photogrammetric mission, GPS units onboard UAVs are used to tag each image with a location. Error in locations from photos includes error from the GPS fix itself, but also in any offset between the GPS and camera location, and as the result of any time synchronization error between the camera and the GPS if they are not integrated. The data produced by the SfM software will then have a similar average error profile as the input GPS. Two approaches are commonly used to correct for these errors. In the first, operators set up distinct targets and locate them precisely with high-accuracy GPS units. These targets are then flagged on input images manually by operators, establishing them as ground control points (GCPs). Typically, at least three – and often far more – GCPs are used on a project to finely register the point clouds and other products to real world coordinates. Alternatively, with the rise of small, UAV-mountable RTK-GPS units such as the Emlid Reach M or Here + RTK, these units can be used for geotagging the images prior to processing, thus increasing the accuracy.

Recent studies (Bolkas 2019; Tomaštík *et al.* 2019; Taddia *et al.* 2020) have demonstrated that although the use of a well-coordinated and executed GCP network with good spatial dispersion throughout the study area produces superior results, onboard RTK-GPS can produce results nearly as good and generally with significantly less cost, as the labor savings of setup for multiple GCPs quickly accumulates. RTK and PPK-based approaches are likely to be of particular benefit at sites where the placement of GCPs is difficult, impractical, or impossible.

Methods

Study area

The study area was located in the northeast section of the Yucatán Peninsula, with individual sites falling within approximately 50 km of Leona Vicario (Figure 1). Many of the sites fell along the Ruta de los Cenotes, a 40 km road that connects Puerto Morelos to Leona Vicario that features many cenotes that have been developed for eco-tourism. Three sites (San Ángel A & B and El Corchal Lake) in the Yalahau Fracture Zone (or Holbox) included atypically large surface water features. In total nine sites were surveyed, including one control site at the coast near Puerto Morelos. This site (UNPM Station) featured a Continuously Operating Reference Station (CORS) near the Universidad Nacional Autónoma de México (UNAM) research site, and provided post-processed GPS correction data via the Continuously Operating Caribbean GPS

Table 1. Description of study sites.

Site	Description
Chichanlub (20.8680, −87.0248)	Deep recreational cenote used for scuba diving along la Ruta de los Cenotes.
El Corchal Lake (21.2720, −87.3495)	Area with surface water, occasionally utilized for eco-tourism.
Leona Vicario (20.9938, −87.2043)	Non-recreational cenote located in Leona Vicario.
Naktunich (20.8356, −87.3237)	Large cenote recently developed for recreation and tourism, not yet open to the public.
San Ángel A (21.2379, −87.3306)	Surface water located in a fracture zone near the town of San Ángel.
San Ángel B (21.2300, −87.4192)	Surface water located in a fracture zone near the town of San Ángel.
UNPM Station (20.8658, −86.8682)	Marine research station located near the coastal city of Puerto Morelos.
Verde Lucero (20.8606, −87.0660)	Popular tourist cenote used for swimming along la Ruta de los Cenotes.
Well Field (20.9268, −87.1314)	Road with wells used for Cancún water supply, located along la Ruta de los Cenotes.

Observational Network (COCONet), now a part of the Network of the Americas (NOTA). Full descriptions of the study sites are given in Table 1, and images of three randomly selected representative sites containing surface water are given in Figure 2.

The next sections detail methodologies for data capture and processing for water surface elevation measurement in the study area. The complete workflow is summarized in Figure 3.

Post-processed kinematic GPS

To establish positions on the ground and at surface water level, we used two Emlid Reach Real Time Kinematic Global Positioning System (RTK GPS) units. The Emlid Reach is a small (3×4.5 cm) portable unit that uses an external antenna (Tallysman TW4721) to receive satellite navigation signals. Although this version of the Reach was capable of transmitting corrections via WiFi (and the now-available M + can transmit via LoRa), we elected to use a post-processing kinematic (PPK) approach with the nearby Puerto Morelos CORS station, since it provided for the best absolute positioning accuracy.

GPS points used in fine positioning/surveying generally utilize a tripod that allows for the external antenna to be placed above ground level. This has the effect of allowing for more satellites to be in view, and therefore improving the accuracy of the signal. In our case, we were interested in taking direct measurements at the water level, which made tripod use impractical. On the water, we placed the RTK GPS unit in a small, sealable plastic container with the antenna securely taped to the lid. The apparatus was tied in place to allow for a static collection. On land, we placed the unit directly on the ground, and in the center of a 50 cm x 50 cm piece of brightly colored cloth that acted as a Ground Control Point (GCP) for the photogrammetry collected with the UAV. On water, the units were placed in a small, buoyant plastic container with antennas mounted externally on the top; containers were secured with lines to prevent drift and movement. On both land and water placements, a 10 cm square metal plate was placed directly beneath the GPS antenna to reduce multi-path interference and improve satellite reception as was recommended in the hardware documentation (Figure 4). The metal plate on the bright cloth, with the antenna placed in the center provided a high contrast surface to aid photogrammetric identification.

Each site generally had more than one subsite. For instance, at Leona Vicario, some RTK GPS placements were on the roof of a nearby abandoned building that served as a launch site. Placing the GPS on the flat roof allowed for very consistent elevation capture. We also sometimes placed a unit directly on the water surface. These two placements represented the two subsites for Leona Vicario. Other sites had a similar differentiation in collection points.

GPS post-processing utilized the RTKPOST software package. It features dozens of settings to fine-tune output, including masking satellites based on angular elevation or signal strength, tropospheric correction method, integer ambiguity resolution, and many more. We experimented with two satellite filtering regimes (filtered and unfiltered) and four different integer ambiguity resolution methods (Continuous, Instantaneous, Fix and Hold, and PPP-AR). Other settings were

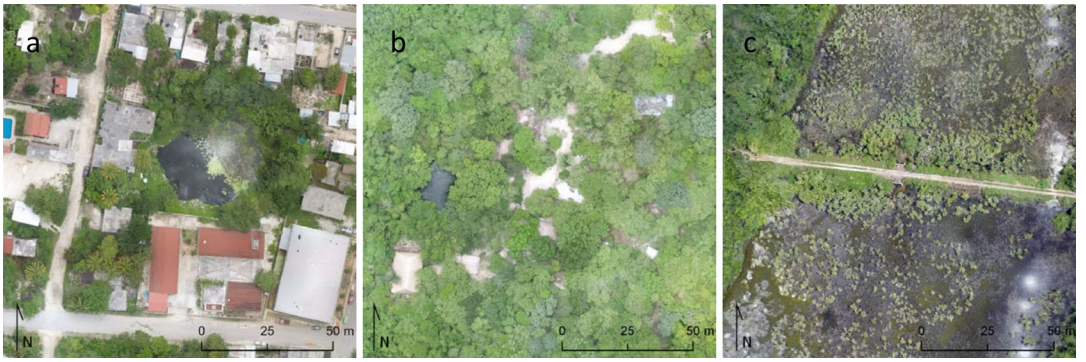

Figure 2. Selected Study Sites: (a) Leona Vicario Domo, a cenote located in an urban area, (b) Verde Lucero, a cenote visited often by tourists, (c) San Angel 1 located in the Holbax fracture zone.

consistent between processing, and in Emlid's post-processing recommendations, including using GPS, GLO, Galileo, QZSS, SBAS, and BeDou satellites, and using Saastamoinen Troposphere correction. The "filtered" processing set used an elevation mask of 15 degrees, and an SNR Mask of 35 dBHz, while the "unfiltered" parameters did not apply these conditions to the processing. The purpose of the filtering in processing was to eliminate "noisy" or unreliable satellites from the position calculation that could decrease accuracy.

Unmanned aerial vehicles

We used two Unmanned Aerial Vehicles for image collection. The first was an off-the-shelf 3DR Iris + quadcopter which weighed 1282 grams, excluding the camera payload. The second was a drone designed by the first-author called the "Busy Bee". The Busy Bee is a lightweight (1137 grams) surveying drone designed to be field-repairable, as the plastic components are all 3 D printable (Figure 5). The frame construction utilized extruded aluminum arms (MakerBeam 1 cm x 100 cm) connected with 3 D printed plastic frame plates. Many of the components were selected to be generally compatible with the Iris+: the batteries, camera, propellers, and mission planning software were all used interchangeably with both models. Electronic components for the custom drone included the top-of-the-line Cube flight controller, the successor to the Pixhawk family of flight controllers. In practice, both models performed similarly in flight, with a maximum safe flight time of approximately 15 minutes. Both models used conventional GPS for aircraft navigation and image tagging; RTK GPS units were used as ground measurement only.

Both models utilized a GoPro Hero 4 Black camera. The GoPro features a 12 mega-pixel (MP) fisheye-type (122.6 degree horizontal x 94.4 degree vertical field of view) image. Camera settings were set in accordance with published recommendations from 3DR. Output images were 4000×3000 pixels.

Missions were generally flown at a variety of elevations, from about 400 feet (~120 m) to 75 feet (~23 m) Above Ground Level (AGL). The nominal ground sampling distance (GSD) or pixel resolution at 120 m is approximately 10 cm with the camera we employed. Images were taken at intervals proportional to flight altitude: at 120 m, images were captured every 4 seconds yielding an overlap (defined as the overlap between images along the flight path) of between 90% and 95%, depending on the orientation of the camera. The Iris + used an adjustable GoPro mounting system in which the camera was oriented horizontally (*i.e.*, the wide body of the camera and the wide edge oriented transversally to the flight path). The Busy Bee used an attachment system where the body of the camera was oriented 90 degrees to the Iris + mounting, where the long edge of the image was parallel to the flight path. Both cameras were pointed straight down (nadir) and were used without a gimbal (ordinarily used to provide stability of the camera,

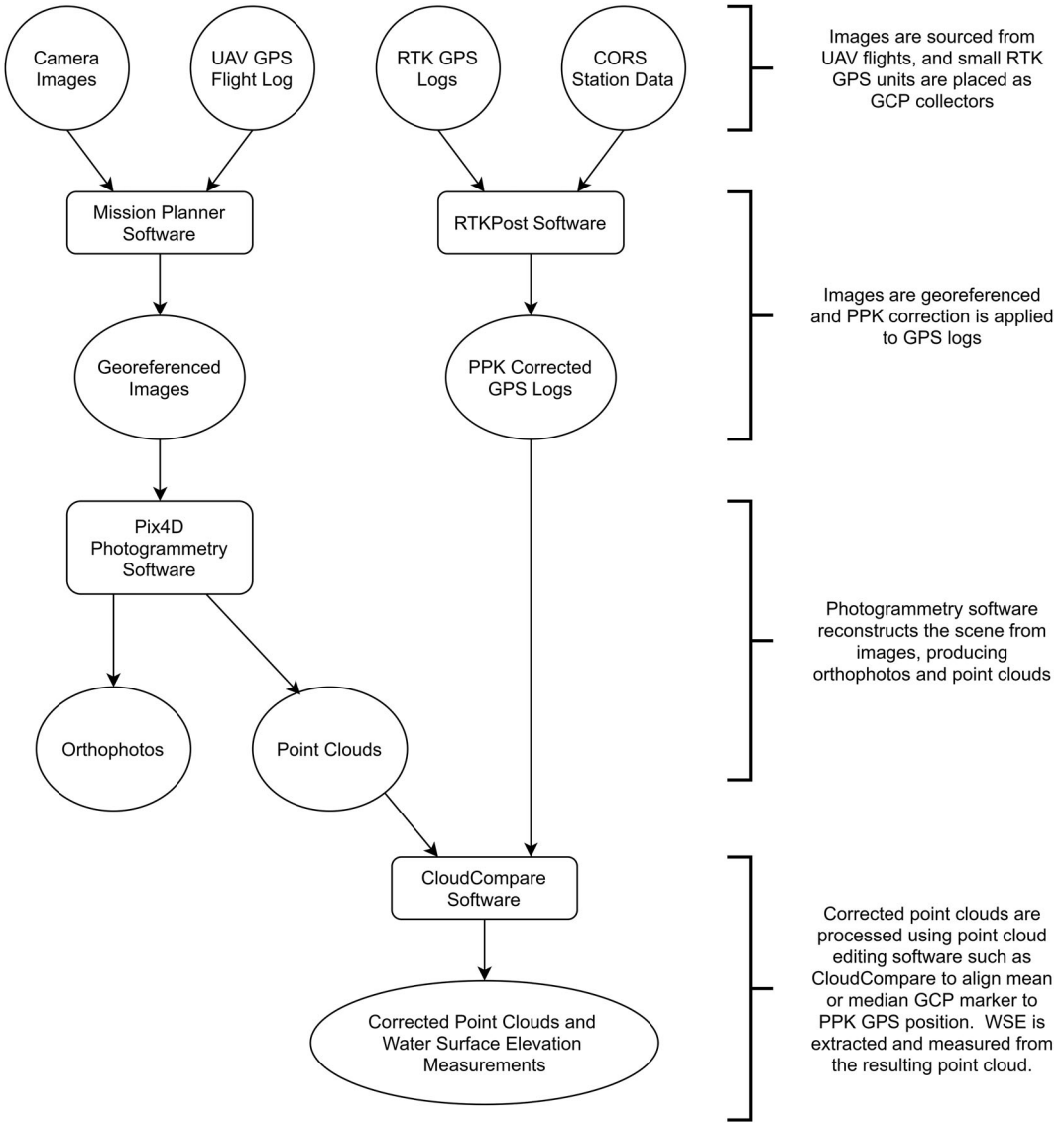

Figure 3. Flowchart describing data processing.

especially for video) in order to minimize weight and maximize flight time. Missions were flown at a speed of 6.5 m per second.

In practice, UAV flying at sites often took at least two hours, given multiple flights and setup and takedown time; our strategy was to maximize RTK GPS collection time by setting up GPS units first, and recovering them last. Once on site and a launch location was chosen, a survey was planned to include the cenote or other key location (well, lake, etc.) as well as the surrounding area. In most cases, each survey at a site included several (2–4) individual flights, with the mission plan influenced by factors that included UAV flight time restrictions/battery capacity and canopy density/visibility. At least two flights were conducted in a sweeping grid pattern, with the second flight orthogonal to the first to form a so-called "double grid" survey pattern to allow for the best 3 D reconstruction. Images were captured by the camera once per second regardless of height, although not all images were used in processing. As a rule, we used one image every four

Figure 4. RTK GPS deployment on water surface (left) and land (right).

Figure 5. 3DR Iris+ (left) and Busy Bee (right).

seconds if the drone flew at 120 m above ground level (AGL), one image every two seconds at 60 m, and 1 image every second at or below 30 m. These mission parameters are summarized in Table 2. As shown, some areas were necessarily flown at higher altitudes for several operational reasons related to vehicle flight time and available number of flights/battery packs.

Since the camera and vehicle were not integrated units, GPS position information was taken from the vehicle's flight log and then applied to the images to georeference them by comparing timestamps using MissionPlanner software. The images were then loaded into the software program Pix4D and processed using standard settings, with the exception that full (rather than the default half) resolution images were used. All output products were registered to the WGS84 UTM 16 N grid, with z-values registered to the WGS84 ellipsoid. Z-values were subsequently transformed to the EGM96 geoid (orthometric) height using an online Geoid Height Calculator published by UNAVCO. Additionally, output products were clipped to a rectangular region surrounding the area of interest, and obvious outliers in the vertical dimension were manually clipped from the point cloud using CloudCompare software.

In total, approximately 7,000 images were taken in the course of 24 individual flights during 13 visits (missions) at 8 sites. The ninth site (El Corchal Lake) could not be flown due to extremely thick canopy cover, with no available breaks to allow for a launch. Additional visits were made to some of these sites for placement of GPS loggers only.

Orientation error in photogrammetric reconstructions

In the environments in which we conducted our field work, dense forest greatly limited our ability, in most cases, for the placement of a large number of Ground Control Points (GCPs) which would ordinarily be standard for this kind of work. One of our aims was to explore alternatives

Table 2. UAV missions and resulting point cloud characteristics.

Mission	# Flights	Flight altitudes (m)	Images	Area (hectares)	Points	Density (rpsm)
Chichanlub	1	60, manual	275	2.0	13,711,777	672.4
Leona Vicario 1	4	30, 30, 120, 20	1,328	2.6	3,812,564	144.2
Leona Vicario 2	1	30	272	2.6	34,045,107	1,304.4
Naktunich	1	120	672	147.0	5,322,315	24.9
San Angel A	1	30	576	0.4	10,846,651	2,543.8
San Angel B	1	30	407	1.6	20,732,312	1,268.8
UNPM 1	1	60	832	7.1	29,694,040	413.7
UNPM 2	1	60	191	5.1	13,403,027	259.3
Verde Lucero 1	4	60, 60, 30, 22	1022	2.6	16,104,225	607.8
Verde Lucero 2	1	60	219	2.6	16,762,450	633.1
Well Field 1	4	120, 120, 120, 120	693	67.0	73,925,663	110.4
Well Field 2	3	120, 120, 120	310	73.1	40,124,663	65.8
Well Field 3	1	120	181	31.8	24,552,411	77.2

to this strategy, by placing one or two GCPs rather than the seven to ten that might be more typical for areas of this size (Bandini *et al.* 2020). Even in flights where images are immediately geolocated, GPS error, time asynchronicities between cameras and GPS units, vehicle placement differences between the GPS and camera, and photogrammetric reconstruction error all play a role in location ambiguity.

Photogrammetric reconstruction typically results in very little bias; that is, objects and scenes are generally reconstructed proportionally correctly, and do not appear "stretched" or "warped" assuming that the camera has been well calibrated in the software. Camera miscalibrations generally result in a noticeable "doming" effect described by James and Robson (2014). One might assume that GPS errors would cancel out over a large area, resulting in a more locationally accurate reconstruction, but this tends not to be the case as GPS error is not purely random (*i.e.*, white noise), but is autocorrelated in time. GPS error can thus be partially modeled as a "random walk" about the true location with the implication that over short time periods such as UAV flights (15–20 minutes), the positional error will "drift" throughout the duration, but not necessarily about the true position. Critically, drift in the z-axis is likely to cause true differences in altitude of the UAV by several meters leading to the appearance of "tilt" or "dip" in the reconstruction. Were this not the case, a single GCP could be used to translate the point cloud to a new corrected position. The empirical question is then to measure the degree of this error and assess the potential impact, given the constraint that the traditional placement of several GCPs is impractical. We use the term "dip" to describe this error, in line with the geological usage of "strike and dip" in which dip refers to the maximum angular tilt.

In order to assess the degree of misorientation in the reconstructed point clouds, we followed two complementary methodologies. First, we used an 11.5 hour GPS record from the grounded Iris + UAV to seed a Monte Carlo simulation, in which random positional drift evident in the logs was used to modify simulated flight paths. Error in the log was typical of most uncorrected GPS errors: horizontal error ($SD_x = 35.1$ cm, $SD_y = 41.8$ cm) was nearly double observed vertical error ($SD_z = 70$ cm).

After fitting a plane to the resulting modified flight path, we could measure the degree of dip from the known true (flat) value. Second, we conducted dozens of actual flights using pre-programmed, precisely similar mission instructions and compared them to several sites whose known positions were all measured using long-term (> 24 hour) static PPK GPS. In addition, we tested and simulated several types of flight, including single grid, double grid, and longitudinal-style and sawtooth-style flight plans (Figure 6) to see if dip variation could be minimized by the choice of flight pattern.

The Monte Carlo simulation used the GPS log to generate 500 simulated flight paths for each of several different variations of flight parameters, including area, shape, and flight type (single or double grid, sawtooth or longitudinal) based on a randomly selected start point in the log. Each

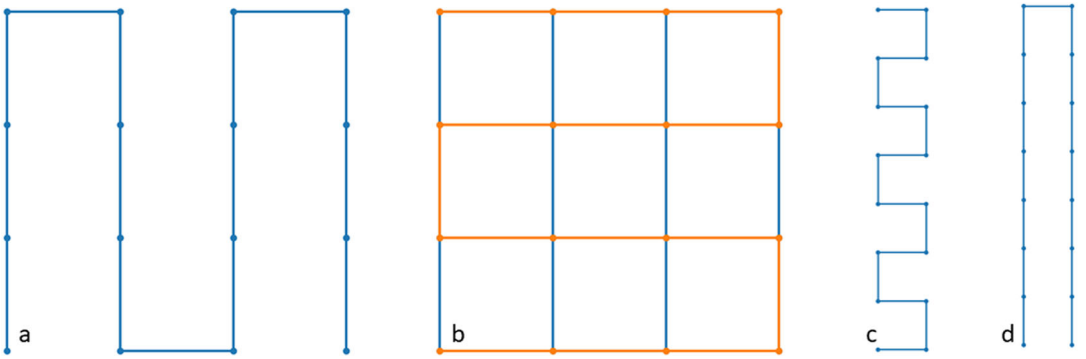

Figure 6. Simulated flight paths for tilt analysis included single grid (of both orientations), double grid, sawtooth, and longitudinal.

flight was simulated with a flight speed of 6.5 m/s, and an image (location) captured every two seconds. A plane was fitted to each simulated flight using a least-squares method implemented in Python, and the dip of the fitted plane was calculated from the result.

A second empirical analysis of dip was conducted with which to compare the results from the Monte Carlo simulation. In this study, the Iris + was flown in a series of 20 separate flights over a 250 m x 100 m (2.5 hectare) area, with waypoints set at 50 m increments. Each flight consisted of both long and short edge (*i.e.*, longitudinal and sawtooth) portions to make a double grid. However, each of these (longitudinal, sawtooth, and double-grid) were processed separately to create a point cloud. CloudCompare's Iterative Closest Point (ICP) algorithm was used to align the cloud to three ground control points gathered using an Emlid Reach RTK GPS, where positions were recorded for 24 hours, and post processed in RTKPOST using the nearby Roanoke Continuously Operating Reference Station (CORS) to establish a PPK fix.

Water level assessment

Given that direct GPS measurement of water levels was unreliable due to poor signal reception, the photogrammetric reconstructions provided the best overall mechanism to assess water levels. Water surfaces themselves do not render well in photogrammetric reconstructions, as there are no stable features of the water itself that the algorithms can use to identify common points. However, reflections will sometimes render as subsurface features, and debris floating on the surface and the water/land interface can be used in the reconstruction.

Water levels were measured by first establishing the vertical difference between the PPK-corrected GCP value and the GCP's location (the 50 cm x 50 cm target) in the point cloud, using a manual extraction in CloudCompare, followed by an inspection of the distribution of z-values as a histogram, where the relative maximum was used to establish elevation. When multiple days' GPS measurements could be reliably combined given the presence of exact position replacement owing to the presence of a marker or exceptionally flat surface such as the Leona Vicario concrete rooftop used for launching, this was done using a weighted average where weights were assigned based on the length of GPS collection time. The original cloud was then translated on the z-axis in CloudCompare using that value. The complete z-adjusted clouds are available online in Potree format at nearearthimaginglab.com/potree/reu2018.

Next, water levels were established by visually inspecting the cenote or other water surface, and then using the manual "segment" tool in CloudCompare to extract the area. Visual signs of the water level included surface features such as floating plant matter, a noticeable "hourglass" structure to the point cloud as reflections rendered under the surface, and other contextual cues. Once extracted, the clouds were statistically inspected in Python using a high-resolution (1 cm

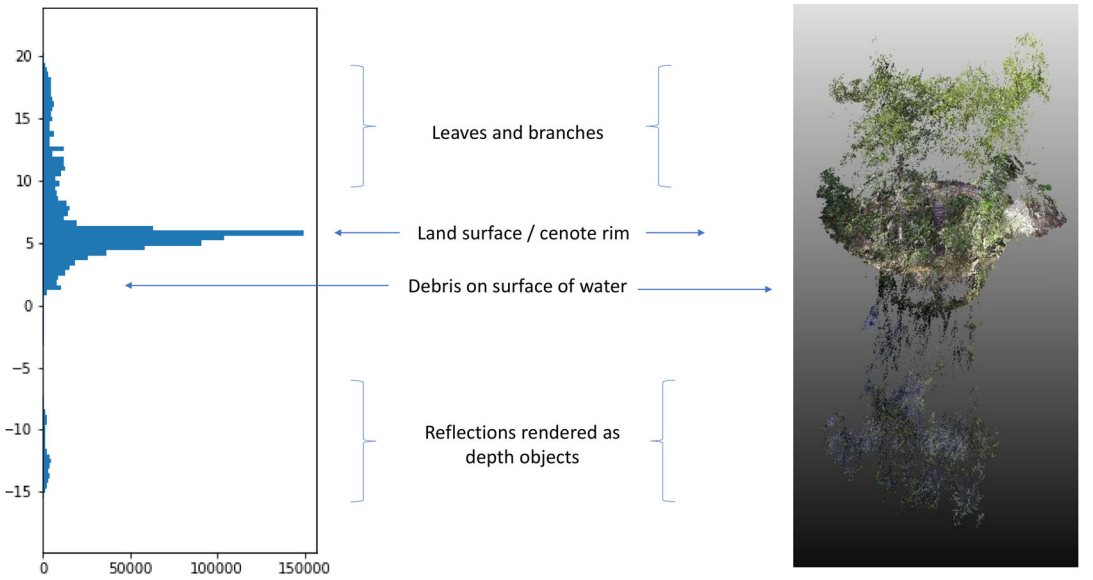

Figure 7. Sample view of using histograms to identify portions of segmented point clouds around cenotes (shown here at Chichanlub).

bin) histogram to find the local maximum of count values; this value was assigned as the water surface elevation (WSE). These values were compared to the calculated mean and median, both giving nearly identical results (within 1 cm), though the median was more robust to outliers. The overall process proved both effective and efficient, with two cycles of manual extraction and statistical inspection taking 10–15 minutes per site. Figure 7 illustrates the process.

Results

Results and individual discussion are provided for several steps of the processing pipeline, with a Discussion presented in the next section. Because of the unusual nature of this study area (low relief and high vegetation density) we provide extensive detail documenting the processing steps to improve reproducibility by other researchers in similar domains. Next, we describe the Structure from Motion reconstructions, the integration of RTK/PPK GPS data, and focus especially on orientation issues in reconstruction – a particularly critical issue for this application. Finally, we integrate these to provide a reconstruction of water surface elevations across the study area.

Flights and photogrammetric reconstruction

As sites varied considerably in their characteristics, there was a good deal of commensurate variability in flight altitudes and areal extents. Some sites such as Leona Vicario and Chichanlub were quite small (2 hectares) while others such as Naktunich and the Well Field were substantially larger (50 to 150 hectares). Mean point cloud density over all sites was 691 returns per square meter (rpsm) but ranged considerably (24.9 to 2,543.8); larger sites required higher flight altitudes to cover, given vehicle battery limitations, and so tended to be imaged more coarsely (Pearson's correlation between area and point density was $r = -0.48$). While our data are not sufficient to speak to how the effect of higher flight altitudes at the larger sites impacted vertical measurement accuracy, Anders *et al.* (2020) found no relationship between flight height and vertical accuracy for UAV-based photogrammetric reconstructions, perhaps because UAVs typically

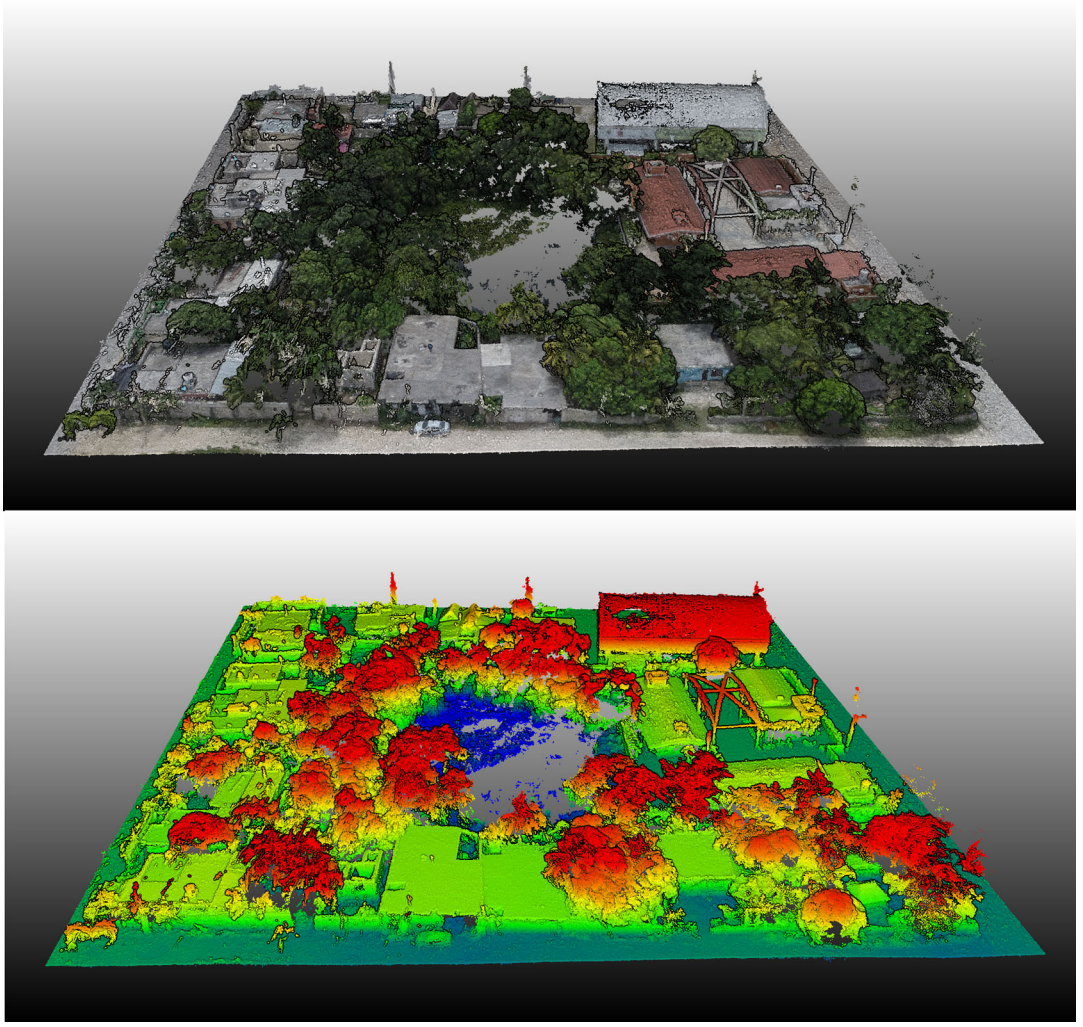

Figure 8. Point cloud renderings (RGB top, z-height bottom) of Leona Vicario cenote (center of images; 20.9938, –87.2043) looking east (up) from launch site ("x"). Length of this city block is approximately 120 m per side.

fly within a relatively narrow range of operational altitudes. As is typical of photogrammetry, areas with well-defined large surfaces and in clear view (*e.g.*, buildings and roads) were reconstructed more faithfully than those without such attributes (*e.g.*, forest canopy). As expected, reconstructions of water surfaces were limited in completeness and tended to be noisy with reflections expressed as subsurface features; the water surface was generally better reconstructed in areas where debris was present and at the water's edge. Figure 8 illustrates a sample point cloud from the Leona Vicario cenote.

As has been noted (Isenburg 2018), photogrammetric and mobile lidar derived point clouds tend to have a "fuzzy" appearance, in which flat, non-permeable surfaces nevertheless have a thickness that Isenburg refers to as "thick ground". This fuzziness in the point cloud was visually evident in all reconstructions, and was directly measurable at Leona Vicario and Verde Lucero, where large, flat cement structures were present. The average of the standard deviation from the median for these four flat surfaces (two missions x two sites) was 8.3 cm, and ranged from 3.95 to 11.5 cm with neither site markedly different than the other. The fuzziness/thickness of photogrammetric point clouds makes registration of such clouds significantly more challenging for

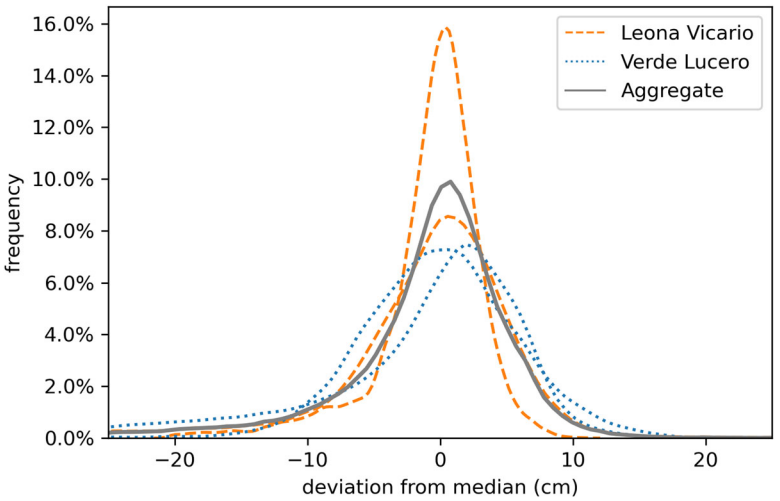

Figure 9. Distribution of deviation from the mean on flat surfaces near GCP collection points. "Fuzziness" in the point cloud is typical of photogrammetric reconstructions.

high-precision applications such as this study, as algorithms to build digital terrain models for instance often will use minimum values within a range or grid cell as "ground" (*e.g.*, Pingel, Clarke, and McBride 2013). Unlike conventional lidar, the z-values within a grid cell around a cluster of photogrammetric points will have a long "tail" of high and low values; and the use of the minimum results in a noisier surface and one in which the bias depends somewhat on the type of surface imaged. In this case, where reconstructions often have relatively normally distributed error (see Figure 9 for plots of deviation about the mean for these flat surfaces), it is likely preferable to tune DTM algorithms to operate on means or medians as reference points rather than maxima and minima. A secondary analysis did not reveal any significant difference in fuzziness when well-located images were tagged with GCPs prior to reconstruction, though very poorly geolocated initial images (position error $>$ 10 m) may see a benefit.

Flights over large extents (Well Field, Naktunich) were necessarily flown at higher altitudes than other, more constrained locations for operational reasons related to vehicle flight time and number of flights possible/number of available battery packs. As a result, these areas were imaged more coarsely (higher point spacing and ground sampling distance). While this similarly increased the thickness or fuzziness of the point cloud at these locations, it does not necessarily impact absolute measurement accuracy there so long as the median value remains near the true value. This is consistent with Anders *et al.* (2020) who reported that higher altitude flights did not statistically significantly decrease feature measurement accuracy.

RTK/PPK GPS evaluation

Our equipment included two single-band Emlid Reach RTK GPS units, which we used in both land and water placements as a comparison point for the photogrammetric reconstruction. Physically, the units were quite small, portable and robust. We had only one logging failure, in which the log did not record for no reason we were able to ascertain. Although we used the units in a somewhat unconventional way, placed directly on the ground or in the water, the accuracy of the units was still commensurate with previously reported values. The length of time of collection greatly impacted the accuracy of the results, with absolute mean vertical error dropping from 17 cm at 15 minutes of collection time to 3.2 cm at 2 hours of collection time (Figure 10). These results were obtained by subsampling a 14-hour log collected as above and analyzed using

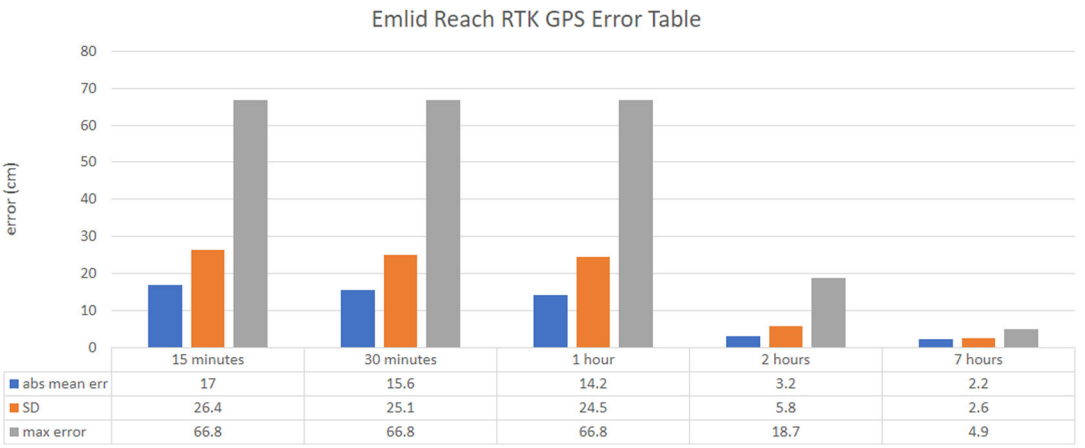

Figure 10. Error profile of Emlid Reach RTK GPS units over time.

RTKPOST software (version 2.4.3 Emlid b28) in a Monte Carlo fashion and comparing the individual subsampled results to the overall result.

Processing of land-placed GPS units benefited slightly from filtering out "noisy" satellites, and benefited substantially from using either Continuous or PPP-AR integer ambiguity resolution (IAR). Figure 11 details the mean error of the on-land RTK GPS placements in Mexico with more than 2 observations per subsite ($n = 19$). The error was calculated as the absolute value of the mean deviation for the algorithmic mean for each subsite. For instance, there were three independent RTK GPS collections for the rooftop at Leona Vicario. A mean elevation for each of the 8 algorithms (2×4), was calculated, and each of the three observations for the subsite was compared to that subsite-algorithm mean. The resulting mean error profile for each algorithm is shown in Figure 11. Excluding satellites based on a poor signal (< 35 dBHz) or being low on the horizon (< 15 degrees) tended to improve results, though only minimally for most algorithms. For the instantaneous algorithm, filtering improved fix precision by an average of 1.5 m (Mann-Whitney $U = 123.0$, $n = 19$, $p = 0.048$). Filtering using the continuous algorithm produced the best overall precision, with mean absolute error equal to 12 cm.

Direct measurement of cenote water levels produced a different error profile. Direct measurement was made at seven sites, but multiple measurements were only possible at two subsites. At both of these sites, unfiltered processing proved much more precise (16 and 12 cm for continuous and PPP-AR, respectively) than filtered processing (5.14 and 3.94 m). Although these results are more suggestive than conclusive, they indicate that as a general rule, continuous and PPP-AR methods are best used without low-signal filtering in these difficult environments. Based on these results, the mean unfiltered continuous score was used for elevation calculation at each subsite. In particularly small-diameter, steep-walled cenotes (*e.g.*, Chichanlub), the direct measurement was clearly in error (measurements ranged from −11.89 to 172.62). However, one indication of this was the large disparity between processing schemes, indicating that bad measurements could be automatically identified and disregarded. At Chichanlub, we took an augmented measurement on a wooden staircase support beam located 2.06 m above the water level, allowing for a reasonably reliable direct measurement there.

Orientation error in photogrammetric reconstructions

The analysis of the Monte Carlo simulation data collected to quantify misorientation in photogrammetric reconstructions identified several key patterns. First, as one might expect, the larger the area surveyed, the less dip there was present. As the horizontal reach of a surveyed area gets

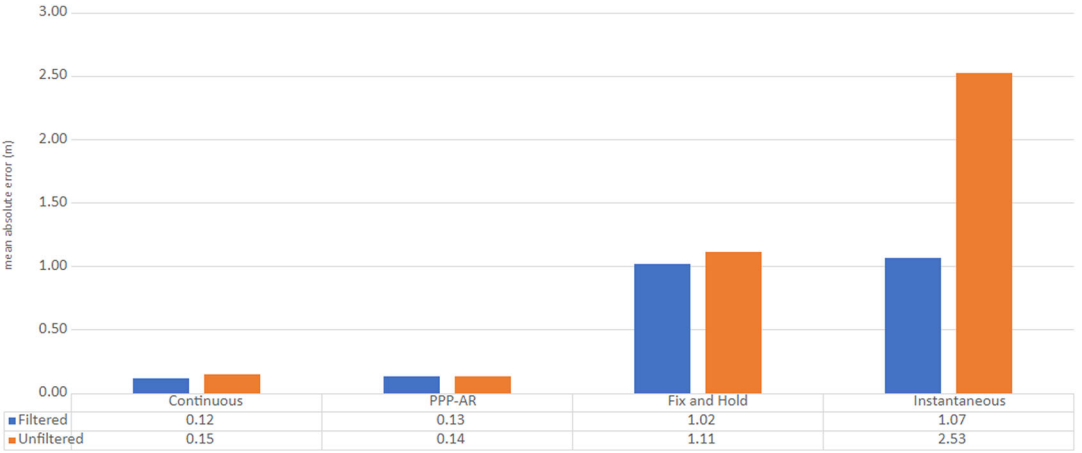

Figure 11. RTKPOST results for land-placed RTK GPS units in Mexico, with more than one observation per subsite.

larger, the vertical component contributing to dip becomes less important. In square-simulated spaces, the median dip was observed to be less than 0.48 degrees when the area was 100 m long per side (1 hectare), but drops to .28 when each side is 200 m long. For non-square, long and thin study areas similar to those flown at the UNPM station and along the Well Field road, simulations showed that sawtooth flights had a much reduced dip over a variety of lengths between 100 and 500 m (median .25 to .75 degrees, with longer lengths showing less dip) when compared to longitudinal flight paths (median 2 to 3 degrees of dip). Double-grid flying tended to improve the median dip by approximately 15–20%, but acted to constrain very high values, dropping the 95th percentile values by approximately 30%.

An analysis of the products resulting from the 20 identical flights revealed that, as one would expect, the double-grid pattern produced the lowest maximum angular dip (median = 0.57 degrees, 95th percentile 0.91). Unlike the simulation, however, sawtooth missions produced slightly *more* dipped reconstructions (median 0.89, 95th percentile 2.1) than longitudinal missions (median 0.69, 95th percentile 0.92). Based on these empirical and simulated data, we conclude that dip in a multiple-mission, double-grid photogrammetric reconstruction is likely to be significantly less than one degree. Any uncorrected dip, however, will result in vertical error increasing away from a single GCP alignment. For this reason, if a single GCP is to be used, it should be placed as close to the target feature to be measured as possible. Within our study area, this was our general practice. At Verde Lucero, for instance, we placed an RTK GPS unit within 25 m of the water's edge. At a dip of .5 degrees this would add an estimated 11 cm of error.

Water level assessment

Cross-checks of the effects of tilted/dipped point clouds mentioned earlier using fitted planes to both the beach near the UNPM station and the long road segment at the Well Field indicated tilts of significantly less than one degree. The estimated orthometric water surface elevations are given in Table 3. Two sites were unable to be reliably calculated. At San Angel B, the RTK GPS record was too short (29 minutes), and did not reliably resolve in post-processing. For this reason we judged the estimate too uncertain to publish. At Verde Lucero, the recreational use of the cenote meant that we were required to fly our UAV at a distance, and could not manually fly the system into the cenote as we were able to do at Chicanlub. In addition, the poor lighting (owing again to the depth), and the lack of vegetation (owing to the recreational use) meant that we could not clearly resolve the surface of the water. Instead, we relied on near features (kayaks, ropes) to establish the WSE. The five surface water measurements (excluding UNPM as a coastal

Table 3. Final Water Surface Elevation (WSE) estimates for non-coastal sites.

Site	WSE (m/EGM96)
Chichanlub	1.61
Leona Vicario	2.52
Naktunich	2.18
San Angel A	2.83
San Angel B	–
Verde Lucero	2.61
Well Field*	1.66

Well Field includes a secondary estimate of water table.

site and San Angel B for reasons outlined above) the mean WSE (above the EGM96 geoid) for the region was measured at 2.35 m ($SD = 0.43$).

Discussion

Water surface elevation (WSE) via UAV typically relies upon a large network of GCPs for fine registration of the point clouds and their derived DEMs (Javernick, Brasington, and Caruso 2014; Woodget *et al.* 2015; Pai *et al.* 2017; Bandini *et al.* 2020). However, in locations where the collection of a large number of GCPs is not feasible due to dense land cover or other factors, our demonstrated PPK-based method of using single GCP can still achieve equivalent decimeter-level accuracy. Our results demonstrated a positional accuracy in dense forest for single-band GPS PPK correction of 12 cm, commensurate with studies conducted in more open environments (Stöcker *et al.* 2017; Forlani *et al.* 2018; Zhang *et al.* 2019). The additional error is attributable to the surrounding dense forest, and we expect that the error values given may help future researchers with more accurate estimates of error budgets. Further, we demonstrated that continuous and PPP-AR based integer ambiguity resolution methods and a minimum of 2 hours of observation time were key elements in minimizing positional error.

The second important consideration in using photogrammetric reconstructions for water surface or other measurements is the spatial bias of the 3 D model, in which "doming" or other systematic distortion occurs (James and Robson 2014; Javernick, Brasington, and Caruso 2014). While we did not observe either convexity or concavity in our reconstructions, the use of a single GCP for registration affords another type of spatial bias not yet discussed in the literature to our knowledge: the problem of "dip" in the reconstruction that happens when minor fluctuations in GPS height of the UAV contribute to a misalignment in the reconstruction. We demonstrated that the magnitude of this tilt is related to the mission plan (*e.g.*, flying in double vs single grid patterns) using both Monte Carlo-based simulation methods as well as extensive repeated identical flights. In practice, this means that when single GCPs are to be used for registration, it is important that the GCP be placed near to the water surface and yet in a place where a clear view of the sky is available to the GPS unit. Our attempt to place RTK GPS units inside cenotes directly on the water surface was unsuccessful, as the deep structures prevented the units from acquiring enough satellite signals to reliably resolve their position. Additionally, the method of using a single GCP for vertical correction only means that horizontal (x,y) and non-linear errors remain, which may affect the accuracy of measurements in other contexts. WSE measurement is less sensitive to this issue than other applications, since water levels are not likely to be meaningfully different within the horizontal error ($\sim$ 2 m) of the reconstructions.

Although SfM-based methods do not image water surfaces directly, many studies have utilized what Bandini *et al.* (2020) refer to as the "water edge" method of measurement in which the boundary of the water surface is first estimated and then the surrounding pixel values of the land surface (*i.e.*, the water's edge) are extracted from a DEM and subsequently used to calculate WSE (Westaway, Lane, and Hicks 2003; Flener at al. 2013; Javernick, Brasington, and Caruso 2014;

Woodget *et al.* 2015; Pai *et al.* 2017). In many of these studies, however, the use of the minimum value within the DEM grid cell can lead to a noisier and more biased surface. The error in SfM point cloud is referred to as "thickness" (Isenburg 2018) or "fuzziness" and is close to normally distributed (shown in Figure 9); as such we recommend that the median value of the grid cell be used for registration after an initial pass of surface features and outliers has been performed using conventional ground filters (Meng, Currit, and Zhao 2010). In fact, while many researchers use off-the-shelf algorithms to create DEMs of point cloud surfaces (Anders *et al.* 2019), we have shown that binning is not a necessary step in WSE extraction and that this can be done directly in point cloud editing software, thus sidestepping any errors introduced in the construction of derivative surfaces. We further suggest that although many studies simply use classification and ground filtering algorithms designed for lidar, the different "thick" character of SfM point clouds suggests that the development of SfM-specific algorithms should be a research priority in the coming years.

The methods described here are manual rather than automatic. In practice, we found marking and extracting WSEs in software with an interface optimized for point cloud processing (CloudCompare) to be quite efficient. However, much of this process could be adapted to automation, including elements of water edge detection (Westaway, Lane, and Hicks 2003; Pai *et al.* 2017), outlier removal (Matkan *et al.* 2014), and more sophisticated statistical binning techniques (Virtanen *et al.* 2020). The additional error associated with the automation will need to be carefully tested and quantified, and weighed against any time savings.

Finally, the WSE measurements presented here indicate very low variation among values quite spatially distant surface water features (SD = 42 cm) with a mild gradient of higher water at more northerly sites. A multi-year project is underway to use these results in concert with other observations about geochemistry and biological contamination to resolve uncertainties in the regional consensus groundwater model (Perry, Velazquez-Oliman, and Socki 2003).

Conclusions

Although laser-based scanning may yet produce more precise results, photogrammetric reconstructions of surface water features show great promise. When combined with RTK/PPK GPS systems, these may be reliably tied to global elevation datums, producing accurate water surface elevation estimates even in demanding areas, such as those surrounded by dense forests. We demonstrated that elevations can be recovered in the point cloud in these environments with an average standard deviation of 8.3 cm, and with an additional PPK GPS error (average *SD*) of 15.1 cm when used in the way described here.

There are additionally several other main findings. First, water surface elevations - known to be poorly modeled using standard methods - are recoverable via photogrammetric point clouds based on analysis of surface detritus. Although we inspected distributions using histograms in Python, such functionality is built into commonly used tools such as ArcGIS Pro and CloudCompare. Second, RTK GPS placement inside cenotes directly on the water surface did not prove effective as the depth to water beneath the surface and steep sides meant that there were not enough GPS satellites in line-of-sight view and multipath errors from the satellites that were in view confused the processing algorithm; as a result, PPK processing did not reliably converge on a solution. On land, PPK was effective, even when placed directly on the ground, with two-hour minimum placement producing noticeably good results. An investigation of various PPK processing schemas demonstrated that Continuous and PPP-AR integer ambiguity resolution made a large positive difference in accuracy. Finally, although the use of many ground control points (GCPs) is still recommended best practice, in areas where such placement is impractical or impossible, good results can still come from the use of even a single GCP when using the manual methods of alignment described here.

Two new technologies show additional promise, and together may solve many of the problems that remain. First, although we elected to use PPK to establish positions, corrections can be directly transmitted to the UAV in real time (as true RTK). However, in order to provide not only enhanced relative accuracy but absolute accuracy, the location of the base unit must be known or otherwise established. Even without absolute positioning, it may be that the relative improvements in positioning help to eliminate nearly entirely the problem of "dip" described. Second, mobile multi-band RTK GPS units are now commercially available (*e.g.*, Emlid Reach M2, released in Spring 2020). These could provide the additional location accuracy when working under the canopy that is needed to further constrain the GPS error.

Acknowledgments

The authors wish to thank Melissa Lenczewski (Northern Illinois University) and Kenneth Voglesonger (Northeastern Illinois University), Principal Investigators on the Research Experience for Undergraduates of this which this research was a part, for their support on the project. We also wish to thank the many researchers at the Centro de Investigación Científica de Yucatán (CICY), most especially Dr. Rosa María Leal-Bautista, for facilitating this research. Finally, we thank the three anonymous reviewers whose comments improved this manuscript.

Funding

This work was supported by the National Science Foundation under Grant number 1852290.

ORCID

Thomas J. Pingel http://orcid.org/0000-0002-5911-2803

References

Anders, N., M. Smith, J. Suomalainen, E. Cammeraat, J. Valente, and S. Keesstra. 2020. Impact of flight altitude and cover orientation on Digital Surface Model (DSM) accuracy for flood damage assessment in Murcia (Spain) using a fixed-wing UAV. *Earth Science Informatics* 13 (2):391–404. doi: 10.1007/s12145-019-00427-7.

Anders, N., J. Valente, R. Masselink, and S. Keesstra. 2019. Comparing filtering techniques for removing vegetation from UAV-based photogrammetric point clouds. *Drones* 3 (3):61. doi: 10.3390/drones3030061.

Andersen, H. E., T. Clarkin, K. Winterberger, and J. Strunk. 2009. An accuracy assessment of positions obtained using survey-and recreational-grade global positioning system receivers across a range of forest conditions within the Tanana Valley of interior Alaska. *Western Journal of Applied Forestry* 24 (3):128–36. doi: 10.1093/wjaf/24.3.128.

Bandini, F., M. Butts, T. V. Jacobsen, and P. Bauer-Gottwein. 2017. Water level observations from unmanned aerial vehicles for improving estimates of surface water-groundwater interaction. *Hydrological Processes* 31 (24): 4371–83. doi: 10.1002/hyp.11366.

Bandini, F., J. Jakobsen, D. Olesen, J. A. Reyna-Gutierrez, and P. Bauer-Gottwein. 2017. Measuring water level in rivers and lakes from lightweight unmanned aerial vehicles. *Journal of Hydrology* 548:237–50. doi: 10.1016/j.jhydrol.2017.02.038.

Bandini, F., A. Lopez-Tamayo, G. Merediz-Alonso, D. Olesen, J. Jakobsen, S. Wang, M. Garcia, and P. Bauer-Gottwein. 2018. Unmanned aerial vehicle observations of water surface elevation and bathymetry in the cenotes and lagoons of the Yucatan Peninsula, Mexico. *Hydrogeology Journal* 26 (7):2213–28. doi: 10.1007/s10040-018-1755-9.

Bandini, F., O. Smith, I. K. Jensen, N. G. Hansted, M. Butts, B. Lüthi, A. G. Photrack, L. Jiang, T. P. Sunding, and P. Bauer-Gottein. 2019. Unmanned Airborne Vehicles (UAVs) for monitoring Danish streams and optimizing river maintenance. Copenhagen. 13th DWF Water Research Conference – Abstracts, 49–50. https://orbit.dtu.dk/en/publications/unmanned-airborne-vehicles-uavs-for-monitoring-danish-streams-and

Bandini, F., T. P. Sunding, J. Linde, O. Smith, I. K. Jensen, C. J. Köppl, M. Butts, and P. Bauer-Gottwein. 2020. Unmanned Aerial System (UAS) observations of water surface elevation in a small stream: Comparison of radar

altimetry, LIDAR and photogrammetry techniques. *Remote Sensing of Environment* 237:111487. doi: 10.1016/j.rse.2019.111487.

Bhang, K. J., and F. Schwartz. 2008. Limitations in the hydrologic applications of C-band SRTM DEMs in low-relief settings. *IEEE Geoscience and Remote Sensing Letters* 5 (3):497–501. doi: 10.1109/LGRS.2008.920712.

Biancamaria, S., D. P. Lettenmaier, and T. M. Pavelsky. 2016. The SWOT mission and its capabilities for land hydrology. *Surveys in Geophysics* 37 (2):307–37. doi: 10.1007/s10712-015-9346-y.

Bolkas, D. 2019. Assessment of GCP number and separation distance for small UAS Surveys with and without GNSS-PPK positioning. *Journal of Surveying Engineering* 145 (3):04019007. doi: 10.1061/(ASCE)SU.1943-5428.0000283.

Brunier, G., J. Fleury, E. J. Anthony, A. Gardel, and P. Dussouillez. 2016. Close-range airborne structure-from-motion photogrammetry for high-resolution beach morphometric surveys: Examples from an embayed rotating beach. *Geomorphology* 261:76–88. doi: 10.1016/j.geomorph.2016.02.025.

Burdziakowski, P., C. Specht, P. S. Dabrowski, M. Specht, O. Lewicka, and A. Makar. 2020. Using UAV photogrammetry to analyse changes in the coastal zone based on the Sopot Tombolo (Salient) Measurement Project. *Sensors* 20 (14):4000. doi: 10.3390/s20144000.

Casas-Beltrán, D. A., C. M. Gallaher, E. Hernandez Yac, K. Febles Moreno, K. Voglesonger, R. M. Leal-Bautista, and M. Lenczewski. 2020. Seaweed invasion! Temporal changes in beach conditions lead to increasing cenote usage and contamination in the Riviera Maya. *Sustainability* 12 (6):2474. doi: 10.3390/su12062474.

Condon, L. E., and R. M. Maxwell. 2015. Evaluating the relationship between topography and groundwater using outputs from a continental-scale integrated hydrology model. *Water Resources Research* 51 (8):6602–21. doi: 10.1002/2014WR016774.

Dandois, J. P., and E. C. Ellis. 2010. Remote sensing of vegetation structure using computer vision. *Remote Sensing* 2 (4):1157–76. doi: 10.3390/rs2041157.

de Roos, S., D. Turner, A. Lucieer, and D. Bowman. 2018. Using digital surface models from UAS imagery of fire damaged sphagnum peatlands for monitoring and hydrological restoration. *Drones* 2 (4):45. doi: 10.3390/drones2040045.

Eltner, A., A. Kaiser, C. Castillo, G. Rock, F. Neugirg, and A. Abellán. 2016. Image-based surface reconstruction in geomorphometry-merits, limits and developments. *Earth Surface Dynamics* 4 (2):359–89. doi: 10.5194/esurf-4-2016.

Fernandes, R., C. Prevost, F. Canisius, S. G. Leblanc, M. Maloley, S. Oakes, K. Holman, and A. Knudby. 2018. Monitoring snow depth change across a range of landscapes with ephemeral snowpacks using structure from motion applied to lightweight unmanned aerial vehicle videos. *The Cryosphere* 12 (11):3535–50. doi: 10.5194/tc-12-3535-2018.

Filhol, S., A. Perret, L. Girod, G. Sutter, T. Schuler, and J. Burkhart. 2019. Time-lapse photogrammetry of distributed snow depth during snowmelt. *Water Resources Research* 55 (9):7916–26. doi: 10.1029/2018WR024530.

Flener, C., M. Vaaja, A. Jaakkola, A. Krooks, H. Kaartinen, A. Kukko, E. Kasvi, H. Hyyppä, J. Hyyppä, and P. Alho. 2013. Seamless mapping of river channels at high resolution using mobile LiDAR and UAV-photography. *Remote Sensing* 5 (12):6382–407. doi: 10.3390/rs5126382.

Forlani, G., E. Dall'Asta, F. Diotri, U. M. di Cella, R. Roncella, and M. Santise. 2018. Quality assessment of DSMs produced from UAV flights georeferenced with on-board RTK positioning. *Remote Sensing* 10 (2):311–22. doi: 10.3390/rs10020311.

Frey, J., K. Kovach, S. Stemmler, and B. Koch. 2018. UAV photogrammetry of forests as a vulnerable process. A sensitivity analysis for a structure from motion RGB-image pipeline. *Remote Sensing* 10 (6):912. doi: 10.3390/rs10060912.

Gesch, D., M. Oimoen, Z. Zhang, D. Meyer, and J. Danielson. 2012. Validation of the international archives of the photogrammetry. *ISPRS - International Archives of the Photogrammetry, Remote Sensing and Spatial Information Sciences* XXXIX-B4:281–6. doi: 10.5194/isprsarchives-XXXIX-B4-281-2012.

Harwin, S., and A. Lucieer. 2012. Assessing the accuracy of georeferenced point clouds produced via multi-view stereopsis from unmanned aerial vehicle (UAV) imagery. *Remote Sensing* 4 (6):1573–99. doi: 10.3390/rs4061573.

Heßelbarth, A., and L. Wanninger. 2013. SBAS orbit and satellite clock corrections for precise point positioning. *GPS Solutions* 17 (4):465–73. doi: 10.1007/s10291-012-0292-6.

Hill, A. C. 2019. Economical drone mapping for archaeology: Comparisons of efficiency and accuracy. *Journal of Archaeological Science: Reports* 24:80–91. doi: 10.1016/j.jasrep.2018.12.011.

Iglhaut, J., C. Cabo, S. Puliti, L. Piermattei, J. O'Connor, and J. Rosette. 2019. Structure from motion photogrammetry in forestry: A review. *Current Forestry Reports* 5 (3):155–68. doi: 10.1007/s40725-019-00094-3.

Isenburg, M. 2018. Median ground models for drone LiDAR from Velodyne puck systems. Accessed May 29, 2020. http://scgi.gistda.or.th/wp-content/uploads/2018/02/SCGI2018-002.pdf.

Isibue, E. W., and T. Pingel. 2020. Unmanned aerial vehicle based measurement of urban forests. *Urban Forestry & Urban Greening* 48:126574. doi: 10.1016/j.ufug.2019.126574.

James, M. R., and S. Robson. 2014. Mitigating systematic error in topographic models derived from UAV and ground-based image networks. *Earth Surface Processes and Landforms* 39 (10):1413–20. doi: 10.1002/esp.3609.
Javernick, L., J. Brasington, and B. Caruso. 2014. Modeling the topography of shallow braided rivers using structure-from-motion photogrammetry. *Geomorphology* 213:166–82. doi: 10.1016/j.geomorph.2014.01.006.
Jiang, S., C. Jiang, and W. Jiang. 2020. Efficient structure from motion for large-scale UAV images: A review and a comparison of SfM tools. *ISPRS Journal of Photogrammetry and Remote Sensing* 167:230–51. doi: 10.1016/j.isprsjprs.2020.04.016.
Jones, K. L., G. C. Poole, S. J. O'Daniel, L. A. Mertes, and J. A. Stanford. 2008. Surface hydrology of low-relief landscapes: Assessing surface water flow impedance using LIDAR-derived digital elevation models. *Remote Sensing of Environment* 112 (11):4148–58. doi: 10.1016/j.rse.2008.01.024.
Leal-Bautista, R. M., M. Lenczewski, G. A. González, and C. G. Hernández. 2019. Evaluation of water quality through the distribution system in Cancún, Mexico. *Sociedad y Ambiente* 8 (21):53–75. doi: 10.31840/sya.v0i21.2039.
Lucieer, A., S. M. D. Jong, and D. Turner. 2014. Mapping landslide displacements using Structure from Motion (SfM) and image correlation of multi-temporal UAV photography. *Progress in Physical Geography: Earth and Environment* 38 (1):97–116. doi: 10.1177/0309133313515293.
Mancini, F., M. Dubbini, M. Gattelli, F. Stecchi, S. Fabbri, and G. Gabbianelli. 2013. Using unmanned aerial vehicles (UAV) for high-resolution reconstruction of topography: The structure from motion approach on coastal environments. *Remote Sensing* 5 (12):6880–98. doi: 10.3390/rs5126880.
Marín, L. E., M. Balcazar, M. Ortiz, B. Steinich, and J. A. Hernandez-Espriu. 2008. Comparison of elevation heights using a Differential Global Positioning System (DGPS) and a Total Station. *Geofísica Internacional* 47 (1):81–3.
Matkan, A. A., M. Hajeb, B. Mirbagheri, S. Sadeghian, and M. Ahmadi. 2014. Spatial analysis for outlier removal from LiDAR data. *ISPRS - International Archives of the Photogrammetry, Remote Sensing and Spatial Information Sciences* XL-2/W3 (2):187–90. doi: 10.5194/isprsarchives-XL-2-W3-187-2014.
McKay, J., M. Lenczewski, and R. M. Leal-Bautista. 2020. Characterization of flowpath using geochemistry and 87Sr/86Sr isotope ratios in the Yalahau Region, Yucatan Peninsula, Mexico. *Water* 12 (9):2587. doi: 10.3390/w12092587.
Meng, X., N. Currit, and K. Zhao. 2010. Ground filtering algorithms for airborne LiDAR data: A review of critical issues. *Remote Sensing* 2 (3):833–60. doi: 10.3390/rs2030833.
Meyer, M., and M. Skiles. 2019. Assessing the ability of structure from motion to map high-resolution snow surface elevations in complex terrain: A case study from Senator Beck Basin, CO. *Water Resources Research* 55 (8):6596–605. doi: 10.1029/2018WR024518.
Munro, P. G., and M. D. L. Melo Zurita. 2011. The role of cenotes in the social history of Mexico's Yucatan Peninsula. *Environment and History* 17 (4):583–612. doi: 10.3197/096734011X13150366551616.
Nesbit, P. R., and C. H. Hugenholtz. 2019. Enhancing UAV–SFM 3D model accuracy in high-relief landscapes by incorporating oblique images. *Remote Sensing* 11 (3):239. doi: 10.3390/rs11030239.
Perry, E., G. Velazquez-Oliman, and L. Marin. 2002. The hydrogeochemistry of the Karst aquifer system of the northern Yucatán Peninsula, Mexico. *International Geology Review* 44 (3):191–221. doi: 10.2747/0020-6814.44.3.191.
Perry, E., G. Velazquez-Oliman, and R. A. Socki. 2003. Socki Hydrogeology of the Yucatán Peninsula A. Gomez-Pompa, M.F. Allen, S.L. Fedick, J.J. Jimenez-Osornio (Eds.), The Lowland Maya: Three Millennia at the Human–Wildland Interface, 115–138. Binghamton, NY: Haworth Press.
Pi-Sunyer, O., and R. B. Thomas. 2015. Tourism and the transformation of daily life along the Riviera Maya of Quintana Roo, Mexico. *The Journal of Latin American and Caribbean Anthropology* 20 (1):87–109. doi: 10.1111/jlca.12110.
Pingel, T. J., K. C. Clarke, and W. A. McBride. 2013. An improved simple morphological filter for the terrain classification of airborne LIDAR data. *ISPRS Journal of Photogrammetry and Remote Sensing* 77:21–30. doi: 10.1016/j.isprsjprs.2012.12.002.
Resop, J. P., L. Lehmann, and W. C. Hession. 2019. Drone laser scanning for modeling riverscape topography and vegetation: Comparison with traditional aerial lidar. *Drones* 3 (2):35. doi: 10.3390/drones3020035.
Rosnell, T., and E. Honkavaara. 2012. Point cloud generation from aerial image data acquired by a quadrocopter type micro unmanned aerial vehicle and a digital still camera. *Sensors (Basel, Switzerland)* 12 (1):453–80. doi: 10.3390/s120100453.
Ryan, J. C., A. L. Hubbard, J. E. Box, J. Todd, P. Christoffersen, J. R. Carr, T. O. Holt, and N. Snooke. 2015. UAV photogrammetry and structure from motion to assess calving dynamics at Store Glacier, a large outlet draining the Greenland ice sheet. *The Cryosphere* 9 (1):1–11. doi: 10.5194/tc-9-1-2015.
Scarelli, F. M., F. Sistilli, S. Fabbri, L. Cantelli, E. G. Barboza, and G. Gabbianelli. 2017. Seasonal dune and beach monitoring using photogrammetry from UAV surveys to apply in the ICZM on the Ravenna coast (Emilia-Romagna, Italy). *Remote Sensing Applications: Society and Environment* 7:27–39. doi: doi: 10.1016/j.rsase.2017.06.003.

Snavely, N., S. M. Seitz, and R. Szeliski. 2008. Modeling the world from internet photo collections. *International Journal of Computer Vision* 80 (2):189–210. doi: 10.1007/s11263-007-0107-3.

Spetsakis, M., and J. Y. Aloimonos. 1991. A multi-frame approach to visual motion perception. *International Journal of Computer Vision* 6 (3):245–55. doi: 10.1007/BF00115698.

Stöcker, C., F. Nex, M. Koeva, and M. Gerke. 2017. Quality assessment of combined IMU/GNSS data for direct georeferencing in the context of UAV-based mapping. *ISPRS - International Archives of the Photogrammetry, Remote Sensing and Spatial Information Sciences* XLII-2/W6:355–61. doi: 10.5194/isprs-archives-XLII-2-W6-355-2017.

Szeliski, R., and S. B. Kang. 1994. Recovering 3D shape and motion from image streams using nonlinear least squares. *Journal of Visual Communication and Image Representation* 5 (1):10–28. doi: 10.1006/jvci.1994.1002.

Taddia, Y., F. Stecchi, and A. Pellegrinelli. 2020. Coastal mapping using DJI Phantom 4 RTK in post-processing kinematic mode. *Drones* 4 (2):9. doi: 10.3390/drones4020009.

Tomaštík, J., M. Mokroš, P. Surový, A. Grznárová, and J. Merganič. 2019. UAV RTK/PPK method—An optimal solution for mapping inaccessible forested areas? *Remote Sensing* 11 (6):721. doi: 10.3390/rs11060721.

Turner, D., A. Lucieer, and C. Watson. 2012. An automated technique for generating georectified mosaics from ultra-high resolution unmanned aerial vehicle (UAV) imagery, based on structure from motion (SfM) point clouds. *Remote Sensing* 4 (5):1392–410. doi: 10.3390/rs4051392.

Turner, I. L., M. D. Harley, and C. D. Drummond. 2016. UAVs for coastal surveying. *Coastal Engineering* 114: 19–24. doi: 10.1016/j.coastaleng.2016.03.011.

Udo, K., S. Takeda, and Y. S. Koshimura. 2018. Detection of coastal damage using differences in automatically generated digital surface models (DSMs): Application to the 2011 off the Pacific coast of Tohoku Earthquake Tsunami. *Journal of Coastal Research* 85:696–700. doi: 10.2112/SI85-140.1.

Verhoeven, G., M. Doneus, C. Briese, and F. Vermeulen. 2012. Mapping by matching: A computer vision-based approach to fast and accurate georeferencing of archaeological aerial photographs. *Journal of Archaeological Science* 39 (7):2060–70. doi: 10.1016/j.jas.2012.02.022.

Virtanen, P., R. Gommers, T. E. Oliphant, M. Haberland, T. Reddy, D. Cournapeau, E. Burovski, P. Peterson, W. Weckesser, J. Bright, et al. 2020. SciPy 1.0: Fundamental algorithms for scientific computing in Python. *Nature Methods* 17 (3):261–72. doi: 10.1038/s41592-019-0686-2.

Wallace, L., A. Lucieer, Z. Malenovský, D. Turner, and P. Vopěnka. 2016. Assessment of forest structure using two UAV techniques: A comparison of airborne laser scanning and structure from motion (SfM) point clouds. *Forests* 7 (12):62. doi: 10.3390/f7030062.

Westaway, R. M., S. N. Lane, and D. M. Hicks. 2003. Remote survey of large-scale braided, gravel-bed rivers using digital photogrammetry and image analysis. *International Journal of Remote Sensing* 24 (4):795–815. doi: 10.1080/01431160110113070.

Westoby, M. J., J. Brasington, N. F. Glasser, M. J. Hambrey, and J. M. Reynolds. 2012. Structure-from-motion' photogrammetry: A low-cost, effective tool for geoscience applications. *Geomorphology* 179:300–14. doi: 10.1016/j.geomorph.2012.08.021.

Wing, M., A. Eklund, and L. D. Kellogg. 2005. Consumer-grade global positioning system (GPS) accuracy and reliability. *Journal of Forestry* 103 (4):169–73. doi: 10.1093/jof/103.4.169.

Womble, J. A., R. L. Wood, and M. E. Mohammadi. 2018. Multi-scale remote sensing of tornado effects. *Frontiers in Built Environment* 4:66. doi: 10.3389/fbuil.2018.00066.

Zhang, H., E. Aldana-Jague, F. Clapuyt, F. Wilken, V. Vanacker, and K. Van Oost. 2019. Evaluating the potential of post-processing kinematic (PPK) georeferencing for UAV-based structure-from-motion (SfM) photogrammetry and surface change detection. *Earth Surface Dynamics* 7 (3):807–27. doi: 10.3929/ethz-b-000364100.